The Influence of Micro- and Macrocracks on the Permeability of Granite

L. Carbillet, L. Griffiths, Michael J. Heap, H. Duwiquet, P. Baud, M. Violay, T. Reuschlé, Laurent Guillou-Frottier

To cite this version:

L. Carbillet, L. Griffiths, Michael J. Heap, H. Duwiquet, P. Baud, et al.. The Influence of Micro- and Macrocracks on the Permeability of Granite. Rock Mechanics and Rock Engineering, 2024, 10.1007/s00603-024-04174-0 . hal-04826278

The Influence of Micro- and Macrocracks on the Permeability of Granite

Carbillet L.[1]*, Griffiths L.[1,2], Heap M.J.[1,3,4], Duwiquet, H.[5], Baud, P.[1], Violay, M.E.S.[4], Reuschlé, T.[1], and Guillou-Frottier, L.[6,7]

[1]*Institut Terre et Environnement de Strasbourg, Université de Strasbourg, CNRS UMR 7063, Strasbourg, France*
[2]*Norwegian Geotechnical Institute, Oslo, 0806, Norway*
[3]*Institut Universitaire Français, Paris, France*
[4]*Laboratory of Experimental Rock Mechanics, École Polytechnique Fédérale de Lausanne, Lausanne, Switzerland*
[5]*Geothermal Division, ENGIE, Paris la Défense, France*
[6]*BRGM, Av. C. Guillemin, BP 36009 45060 Orléans Cedex 2, France*
[7]*Univ. Orléans, CNRS, BRGM, ISTO, UMR7327, 45071 Orléans, France*

*Corresponding author: L. Carbillet (lcarbillet@unistra.fr)

ORCID

Carbillet L.: 0000-0001-6245-3679
Griffiths L.: 0000-0002-7546-2571
Heap M.J.: 0000-0002-4748-735X
Duwiquet, H.: 0000-0003-0278-3005
Baud, P.: 0000-0002-4728-7649
Violay, M.E.S.: 0000-0002-7402-8263
Reuschlé, T: 0000-0002-0490-5072
Guillou-Frottier, L: 0000-0002-2698-1447

Statements and Declarations

The authors declare that they have no financial or proprietary interests in any material discussed in this article.

Acknowledgements and Funding

The authors of this study acknowledge funding from ANR project GERESFAULT (ANR-19-CE05-0043). M.J. Heap and M.E.S. Violay acknowledge funding from a Hubert Curien Partnership (PHC) Germaine de Staël grant (number 47712SB), implemented by the Swiss Academy of Technical Sciences (SATW) and the State Secretariat for Education, Research, and Innovation (SERI) in Switzerland, and the Ministry for Europe and Foreign Affairs (MEAE) and the Ministry for Higher Education, Research, and Innovation (MESRI) in France. This work was also supported by European Research Council Starting Grant BEFINE (ERC-2017-STG), awarded to M.E.S. Violay. This work of the Interdisciplinary Thematic Institute GeoT, as part of the ITI 2021-2028 program of the University of Strasbourg, CNRS and Inserm, was supported by IdEx Unistra (ANR-10-IDEX-0002), and by SFRI-

STRAT'US project (ANR ANR-20-SFRI-001) under the framework of the French Investments for the Future Program (PIA). M.J. Heap acknowledges support from the Institut Universitaire de France (IUF). We thank Bertrand Renaudie and Laurent Gastaldo for technical support.

Author Contributions

Study conceptualization and design were performed by Lucille Carbillet and Michael J. Heap. Material preparation and data collection were performed by Luke Griffiths and Michael J. Heap. Formal analysis was performed by Lucille Carbillet, Luke Griffiths, Michael J. Heap and Patrick Baud. Modelling was performed by Hugo Duwiquet and Laurent Guillou-Frottier. Funding and resources were acquired and provided by Michael J. Heap, Marie Violay and Laurent Guillou-Frottier. The first draft of the manuscript was written by Lucille Carbillet, Michael J. Heap, Luke Griffiths and Hugo Duwiquet. All authors commented on successive versions of the manuscript. All authors read and approved the final manuscript.

Highlights

- Microcracks start forming in Lanhélin granite around 100°C, making the rock samples progressively more porous and permeable but weaker up to 700°C.
- Under compression, the permeability of microcracked samples initially drops due to closing microcracks and then increases to a residual level when a large fracture forms.
- During pre-failure deformation in the brittle regime, the permeability of our microcracked granite decreases whereas that of initially intact granite increases.

Abstract

Damage zones exist around crustal faults, where micro- and macrocracks coexist and form a complex conduit network for fluid flow. The permeability of these zones can change rapidly as the crack network evolves during deformation. To investigate the relative influence of micro- and macrocracks on permeability, we performed an experimental study on Lanhélin granite, consisting of three steps: (1) monitoring thermal microcracking using high-temperature experiments, (2) measuring the evolution of physical properties following thermal stressing, and (3) measuring the permeability of thermally-stressed samples during triaxial deformation. By monitoring acoustic emission activity and P-wave velocity during heating, we find that thermal microcracking starts at ~100 °C and accumulates up to the maximum temperature of 700 °C. Porosity and permeability increase and P-wave velocity, uniaxial compressive strength, and thermal conductivity and diffusivity decrease as thermal stressing temperature increases from room temperature to 700 °C. The axial permeability of thermally-stressed samples decreases by about one order of magnitude during triaxial loading to the peak stress, due to the closure of pre-existing microcracks, and then increases following the formation of a macroscopic shear fracture. Permeability then remains more-or-less constant as strain is accommodated by

on the resultant shear fracture. Our results show that the permeability of microcracked granite evolves differently to intact granite, for which permeability increases, during pre-failure deformation in the brittle regime. Such results have important implications for fluid flow in crustal fault systems and their potential for geothermal energy exploitation, which we explore using a simple numerical simulation.

Keywords: Microcrack; Macrocrack; Permeability; Granite; Acoustic emissions

1. Introduction

Cracks exist on a variety of scales, from microcracks on the millimetric scale (Kranz 1983) to crustal-scale faults that can be over 1000 km long (e.g., the San Andreas Fault, USA; Anderson 1971). Micro- and macrocracks are capable of significantly influencing the physical and mechanical properties of rock and rock-masses. Microcracks can decrease the strength and stiffness (David et al. 2012; Wang et al. 2013; Chen et al. 2017; Li et al. 2020; Xu et al. 2023), increase permeability (David et al. 1999; Darot and Reuschlé 2000; Chaki et al. 2008; Feng et al. 2021), decrease P-wave velocity (Reuschlé et al. 2006; Nasseri et al. 2007; Chen et al. 2017; Pimienta et al. 2019), and decrease thermal conductivity (Kant et al. 2017; Zhao et al. 2018) of granite. For example, Griffiths et al. (2017) found that the uniaxial compressive strength of a fine-grained granite decreased from ~290 to ~120 MPa as the number of microcracks per unit area increased from ~80 to ~160 mm^{-2}. David et al. (1999) found that mechanically- and thermally-induced microcracks can increase the permeability of initially intact granite by up to four orders of magnitude. In terms of macroscopic cracks, Villeneuve et al. (2018) showed that the presence and number of macrocracks can significantly reduce the strength of a granitic rock. Mitchell and Faulkner (2008) and Nara et al. (2018) found, respectively, that the presence of a macroscopic shear and tensile fracture can increase the permeability of granite by up to three to four orders of magnitude.

Permeability–the ease at which fluid can flow through a porous medium—influences the distribution of pore fluids and pore fluid pressure and therefore exerts a significant influence over crustal faulting and earthquakes (Sibson 1996; Jónsson et al. 2003; Wang and Manga 2021). As a result, the permeability of fault rocks and the permeability distribution in fault zones have been closely scrutinised (Caine et al. 1996; Rawling et al. 2001; Faulkner et al. 2010). The permeability of crustal rocks and rock-masses also dictates the efficiency of hydrothermal circulation (Hicks et al. 1996; Guillou-Frottier et al. 2013; Vallier et al. 2019; Duwiquet et al. 2019; Bauer et al. 2019) and therefore the productivity of geothermal resources (Huenges and Ledru 2011). Pore pressure perturbations can also create unwanted induced seismicity during geothermal production (Goertz-Allmann et al. 2011; Terakawa et al. 2012) and the flooding and failure of underground engineered spaces (Yin et al. 2015).

Many of the experimental studies that have sought to measure the permeability of granite during triaxial deformation, such as Mitchell and Faulkner (2008), provide permeability data up to or immediately following the formation of a macroscopic shear fracture. Experiments have also typically been performed on intact granite samples that initially contain very few microcracks while, in many crustal settings, such as fault zones (Mitchell and Faulkner 2012) and geothermal reservoirs (Genter and Traineau 1996), granite can contain abundant microcracks. In this study, we provide a comprehensive experimental dataset for the evolution of physical properties of microcracked granite – representative of rocks found in damage zones adjacent to faults – under elevated pressure and temperature representative of crustal conditions. Therefore, we present a suite of triaxial deformation experiments, performed at different effective pressures, in which we measured the permeability of microcracked granite samples to high strains in the brittle field. We complement these data with experiments in which we measured the output of acoustic emissions, considered a proxy for microcrack growth (Lockner 1993), and the P-wave velocity of granite during heating and cooling, and experiments in which we measure the physical properties (porosity, permeability, P-wave velocity, thermal properties, and uniaxial compressive strength) of granite following exposure to high temperatures (up to 700 °C). Finally, we examined fluid flow characteristics within a crustal fault system through a simple numerical simulation parameterised using our experimental results.

2. Materials and methods

2.1 Experimental material: Lanhélin granite

We used Lanhélin granite for our experiments, a coarse-grained, blue-grey granodiorite from Brittany (France). Lanhélin granite contains predominantly quartz, feldspar, and mica, and has an average crystal size of ~1 mm (Fig. 1). It was selected here due to its previous use in studies of rock physical properties and rock deformation (Siratovich et al. 2015; Chandler et al. 2017; Wadsworth et al. 2017; Yu et al. 2021). In addition, Lanhélin granite is particularly interesting to study the influence of cracks on permeability because it is prone to forming high-aperture microcracks during thermal stressing (Griffiths et al., 2017). All the samples used in this study (13 in total) were prepared from the same block of Lanhélin granite.

2.2 Physical property measurements of thermally-stressed samples

A suite of Lanhélin granite samples, 20 mm in diameter and nominally 40 mm in length, were thermally-stressed in a furnace at room pressure up to target temperatures of 100 (sample LG2), 200 (LG3), 300 (LG4), 400 (LG5), 500 (LG6), 600 (LG7), and 700°C (LG8). For each target temperature, one sample was heated up at a rate of 1 °C/min and left at the target temperature for two hours, and finally cooled down to room temperature at 1 °C/min. We then measured the connected porosity, P-wave velocity, permeability, thermal diffusivity, thermal conductivity, and uniaxial compressive strength (UCS) of the thermally-stressed samples at room temperature. The evolution of physical properties in granite with temperature was not the focus of this study and therefore permeability, UCS and thermal properties were voluntarily measured only for selected thermal stressing temperatures. For each target temperature, one thermally-stressed sample served to measure all the physical properties. We also measured the physical properties of an intact sample (i.e., a sample that was not thermally-stressed, sample LG1). In total, 8 granite samples were used for these measurements.

Connected porosity was measured at room pressure and temperature using the skeletal volume measured by a helium pycnometer (AccuPyc II 1340) and the bulk sample volume measured by digital callipers. P-wave velocity was measured using a digital oscilloscope and a pulser/receiver at room pressure and temperature along the length of the samples. P-wave velocities were derived using the length of the rock samples and the travel time of a single period sinusoidal signal with a frequency of 700 kHz through the samples, where P-wave arrival times were picked manually on the oscilloscope. To ensure reproducibility, P-wave velocities were measured under an axial load of 300 N. Permeability was measured using a benchtop gas permeameter (see Heap and Kennedy (2016); Farquharson et al. (2016) for a schematic of the experimental device) using either the pulse-decay method (for low permeability samples) or the steady-state method (for high permeability samples). Permeability measurements were made at room temperature, under a confining pressure of 1 MPa, using nitrogen as both the permeant and confining gas. When required, Darcian permeability values were corrected for the effects of fluid-flow related artefacts, i.e., turbulent flow, known as the Forchheimer effect, and gas slip along flow channel walls, known as the Klinkenberg effect (see Heap et al. (2017) for a detailed presentation of the equation used). Thermal diffusivity and thermal conductivity were measured at room pressure and temperature using a Hot Disk® TPS 500 Thermal Constants Analyser using the transient plane source method (Gustafsson 1991; Gustavsson et al. 1994; Harlé et al. 2019; Heap et al. 2020, 2022a). Uniaxial compressive strength (UCS) was measured at room pressure and temperature using a uniaxial loadframe (schematics provided in Heap et al. 2014). For each UCS test, the load was applied through an axial steel piston advanced onto the tested sample at a constant displacement rate corresponding to a strain rate of 10^{-5} s^{-1}. The displacement of the piston, monitored using an external linear variable differential transducer (LVDT), was used to derive axial strain. The axial force was measured by a load cell and converted into axial stress using the cross-sectional area of the tested sample. Samples were deformed until macroscopic failure. UCS values correspond to the axial stress at the peak of the stress-strain curves obtained.

2.3 Output of acoustic emissions and P-wave velocity evolution during heating and cooling

In the following, we will use *in-situ* to refer to measurements performed live, directly in the experimental apparatus during the heating-cooling cycles. These measurements differ from those made at room temperature on samples that have been heated to a target temperature and cooled back to room temperature, referred to as thermally-stressed samples.

In-situ measurements of acoustic emissions (AE) were performed on a granite sample (20 mm in diameter and nominally 40 mm in length, sample LG9) during a heating-cooling cycle to 700 °C. The sample was placed in a uniaxial loading frame specifically designed for high-temperature AE measurements (described in detail in Griffiths et al. (2018)) between two vertical stainless-steel pistons, and a tube furnace (GSL 1100X) was mounted around the assembly. The use of a uniaxial load frame served not to deform the samples but to apply a small load ensuring good coupling between the measured sample and the piston and transducers while also improving the repeatability of the measurements. In this apparatus, a broadband acoustic sensor (a micro80 miniature sensor from Physical Acoustics with a bandwidth of 200–900 kHz) is embedded into the upper piston, the top of which is attached to a load cell. The temperatures of the cell and the AE transducer are kept at room-temperature using a specifically designed air-cooling system to avoid damage due to exposure to high temperatures. During the thermal stressing cycle, a load of 100 N was applied using the servo-controlled upper piston to ensure a constant coupling between the granite sample and the AE sensor. As the temperature of the tube furnace was elevated from room conditions to 700°C and back, AE hits were recorded using a USB AE Node from Physical Acoustics connected to the AE sensor. The software AEwin was used to monitor the AE activity, with a detection threshold for an AE hit set to 40 dB.

The same experimental setup (equipped with different platens and transducers) was used to measure in-situ P-wave velocity on another granite sample (20 mm in diameter and nominally 40 mm in length, sample LG10) during a heating-cooling cycle to 400 °C. For these measurements, a high-temperature acoustic sensor (S9215 from Physical Acoustics with a resonant frequency of 100 kHz and an operating frequency of 80–560 kHz) was placed at the end of the upper piston in contact with the sample, to serve as the source of the acoustic signal, and another one was placed at the end of the lower piston in contact with the sample to serve as the receiver. The maximum temperature for in-situ P-wave velocity measurements was limited to 400 °C due to the operating range of the acoustic transducers used in the furnace.

To summarize, P-wave velocities and the output of AE activity were measured during heating and cooling, as described here above, whilst measurements of the physical properties (e.g., porosity, thermal properties, etc.) were measured on room-temperature samples that had been heated to and cooled from a target thermal stressing temperature (see section 2.2).

2.4 Permeability evolution during deformation in the brittle regime

Three cylindrical samples of Lanhélin granite, 37 mm in diameter and 75−80 mm in length (samples LG11-13), were prepared for permeability measurements during deformation in compression under triaxial conditions. To create a network of microcracks within the sample, and to ensure that the permeability was measurable on reasonable laboratory timescales, we first thermally-stressed these three samples to 700 °C at room pressure. Similar to the experiments described above, these samples were first heated to 700 °C at a rate of 1 °C/min, left at 700 °C for two hours, and finally cooled down to room temperature at 1 °C/min.

To ensure that the shear fractures which formed in the samples during the triaxial deformation experiments (described below) were oriented at the same angle with respect to the maximum principal stress and facilitate the comparison between the data from the different experiments, we cut two 1 mm-wide and 4 mm-deep notches on opposite sides of the sample. These notches, orientated at 30° to the maximum principal stress, were made using a precision saw (Secotom Precision Cutting Machine from Struers) and were then filled with a liquid silicone rubber that hardens at room temperature to prevent the confining pressure from puncturing the Viton© jacket.

Deformation experiments were performed on these samples using the FIRST (Fluid Induced eaRthquake SimulaTor; see Noël et al. 2021; Heap et al. 2022b) triaxial apparatus at the Laboratory of Experimental Rock Mechanics (Ecole Polytechnique Fédérale de Lausanne, Lausanne, Switzerland). Prior to deformation, the samples were vacuum-saturated with deionised water. For each triaxial test, the sample to-be-deformed was placed between two 5 mm-thick pore-fluid spreader plates, slid inside a Viton© jacket, and the whole assembly was mounted inside a pressure vessel (schematic provided in the Supplementary Information). Two separated pairs of servo-controlled pumps were used to control the pressure of the confining fluid (oil), Pc, and that of the pore fluid (deionised water), Pp. The experiments were performed at effective pressures $Peff$ of 10, 30, and 50 MPa, with a constant pore pressure of 10 MPa, and assuming a simple effective pressure law $Peff = Pc - Pp$.

At the beginning of each test, the confining pressure and the pore pressure were increased to their target values using the servo-controlled pumps and the system was left to equilibrate. Following microstructural equilibration, axial loading was applied by lowering an axial piston on the sample at a constant displacement rate, corresponding to an axial strain rate of 10^{-5} s^{-1}. The position of the piston was controlled and recorded using an external LVDT attached to its top. Two internal LVDTs and the initial sample length were used to calculate axial strain, while the pressure acting on the piston and the initial sample cross-section were used to calculate axial stress. Differential stress was corrected for the friction at the interface between the axial piston and the walls of the apparatus column. During deformation, only one pore pressure pump was used to maintain a pressure of 10 MPa, while the other pump was disconnected from the circuit in order to ensure accuracy in the measurement of the pore volume change. The porosity change was calculated from the change in pore volume (given by the displacement of the piston in the pore pressure intensifier during the experiment) and the initial bulk sample volume. During deformation, fully drained conditions were ensured at the imposed strain rate given the permeability and dimensions of the samples.

During each triaxial test, the permeability of the sample was measured first under hydrostatic conditions (before any axial loading was applied) and then intermittently during deformation. The permeant fluid for these permeability measurements was the pore fluid, i.e., deionised water. For each permeability measurement, the loading was halted (except for the first measurement under hydrostatic conditions) and both the upstream and downstream pore fluid pumps were connected to the circuit. The upstream pore pressure pump was set at 10.1 MPa while the downstream one was set at 9.9 MPa so that a pore pressure difference of 0.2 MPa was imposed between the two ends of the sample. The resulting movement of water through the sample was tracked and the corresponding volumetric flow rate was used to calculate permeability using Darcy’s law. Steady-state flow, i.e., when the displacement of the upstream and downstream pore pressure pumps was constant, was typically achieved in several minutes. After several tens of minutes at constant flow rate, one of the pore pressure pumps was isolated from the pore pressure circuit while the other was set back to a constant pore pressure of 10 MPa and loading was continued. During all three triaxial tests, permeability was measured using this method up to an axial strain of 0.09−0.10. A detailed example of the method used to compute permeability is presented in the Supplementary Information (as an accompanying Excel file). Permeability measurements were conducted along the axial direction of the cylindrical samples only (not along the fracture plane generated during triaxial compression) and considered the change in sample length. The permeability values obtained correspond to the equivalent permeability of the bulk samples which, at certain stages of the deformation, can include the contributions of the potentially more permeable fracture and less permeable matrix. In the following, we will refer to our bulk axial permeability data simply as *permeability*. It should be noted that the measured permeability represents a lower bound permeability since microcracks in the rock samples likely undergo relaxation when loading is halted to perform the measurements.

3. Results

3.1 Petrophysical and microstructural evolution during thermal stressing

The porosity, P-wave velocity, permeability, uniaxial compressive strength, thermal diffusivity, and thermal conductivity of Lanhélin granite are plotted as a function of thermal-stressing temperature in Fig 2. These data show that porosity and permeability increase, whereas P-wave velocity, uniaxial compressive strength, thermal diffusivity, and thermal conductivity decrease as a function of thermal-stressing temperature (Table 1). All of the measurements in this section were performed at room temperature on samples that had been heated to and cooled from a target thermal stressing temperature.

Increases in porosity start at a thermal-stressing temperature above 200 °C (Fig. 2a). Porosity is increased from ~0.005 to ~0.01 as thermal-stressing temperature is increased from 200 to 500 °C. Increases in porosity are much greater at temperatures above 500 °C and porosity increases from ~0.01 at 500 °C to ~0.03 at 700 °C. P-wave velocity decreases more-or-less linearly as thermal-stressing temperature is increased from room temperature up to 700 °C (Fig. 2b). P-wave velocity is reduced from ~6 km/s at room temperature down to ~1.5 km/s at a thermal-stressing temperature of 700 °C. Permeability increases exponentially as a function of thermal-stressing temperature (Fig. 2c). Permeability increases from ~10^{-20} m^2 at room temperature to ~10^{-14} m^2 at a thermal-stressing temperature of 700 °C, an increase by about six orders of magnitude, at ambient pressure. Uniaxial compressive strength remains quasi constant at a thermal-stressing temperature of 300 °C (uniaxial compressive strength is ~150–160 MPa) (Fig. 2d). At a thermal-stressing temperature of 700 °C, the uniaxial compressive strength is decreased from ~150–160 MPa to ~65 MPa. Mechanical data for the UCS tests are available in Supplementary Information. Thermal conductivity and thermal diffusivity remain almost unchanged to a thermal-stressing temperature of 300 °C (Figs. 2e and 2f). Above a thermal-stressing temperature of 300 °C, thermal conductivity and thermal diffusivity decrease up to the maximum thermal-stressing temperature of 700 °C. Thermal diffusivity decreases from ~2 $mm^2 \cdot s^{-1}$ at temperatures of 25–300 °C to ~1 $mm^2 \cdot s^{-1}$ at a thermal-stressing temperature of 700 °C. Thermal conductivity decreases from ~3–3.5 $W \cdot m^{-1} \cdot K^{-1}$ at temperatures of 25–300 °C to ~1.75 $W \cdot m^{-1} \cdot K^{-1}$ at a temperature of 700 °C.

Cumulative AE hits and P-wave velocity, measured under in-situ conditions, as a function of temperature during the thermal-stressing of samples of Lanhélin granite are shown in Fig. 3 (these data were collected on different samples, but we show them here together for ease of comparison). We note that the output of AE activity during the heating of the sample starts at ~100 °C (solid red line). The number of AE hits increases as a function of temperature above ~100 °C, more rapidly above ~450 °C and then with a noticeable increase at a temperature of ~550–600 °C. During the cooling of the sample, there is a steady increase in the number of AE hits from 700 °C down to room temperature (solid blue line). In-situ P-wave velocity decreases during the heating of the sample, the rate of which increases as the sample is heated above ~100 °C (dashed red line). During heating to 400 °C, the P-wave velocity of the sample is reduced from ~6 km/s down to ~3 km/s. During cooling, the P-wave velocity of the sample increases from ~3 km/s at a temperature of 400 °C to ~3.5 km/s at room temperature (dashed blue line).

We also determined the microcrack surface area per unit volume and the 2D microcrack density for samples of Lanhélin granite thermally-stressed to 300 and 700 °C, as well as for an intact sample. Optical microscope images of intact Lanhélin granite, and samples thermally-stressed to 300 and 700 °C, are shown in Figs. 4a, 4b, and 4c, respectively. Qualitatively, we observe an increase in the number of microcracks as the sample is thermally-stressed to 300 and 700 °C. We calculate the microcrack surface area and the 2D microcrack density for each of these images using the automated segmentation procedure for optical micrographs presented and described in Griffiths et al. (2017). These results are presented in Fig. 4d. We find that the microcrack surface area increases from ~0.8 mm^{-1} at room temperature to ~6 mm^{-1} at a thermal stressing temperature of 700 °C (white circles). 2D microcrack density increases from ~0.025 to ~0.17 as thermal-stressing temperature is increased from room temperature to 700 °C (blue diamonds).

3.2 Mechanical data and permeability changes in the brittle regime

In the following, we adopt the convention that compressive stress and compactive strain are positive. We will first describe the evolution of porosity and permeability under hydrostatic conditions (up to 50 MPa), before describing the mechanical data and the evolution of porosity and permeability as a function of axial strain (at effective pressures of 10, 30, and 50 MPa).

The evolution of porosity and permeability as a function of effective pressure is shown in Figs. 5a and 5b, respectively (data available in Table 2). We find that porosity and permeability decrease non-linearly as a function of increasing effective pressure. In both cases, the decreases in porosity and permeability per unit effective pressure are larger at low effective pressure. Over the entire pressure range (up to 50 MPa), porosity decreased by ~0.008 and permeability decreased from 6.9×10^{-16} m^2 at an effective pressure of 2 MPa to 5.3×10^{-18} m^2 at an effective pressure of 50 MPa.

The stress-strain curves and porosity change as a function of axial strain for the three triaxial experiments (at effective pressures of 10, 30, and 50 MPa) performed on thermally-stressed samples of Lanhélin granite are shown in Figs. 6a and 6b, respectively. The three experiments can all be classed as brittle: the stress increases to a maximum (the peak stress), followed by a stress drop associated with macroscopic sample failure (the formation of a shear fracture). Following fracture formation, the stress remained more-or-less constant as deformation was accommodated by sliding on the formed fracture. While differential stress increases almost linearly to a maximum, porosity change decreases (compaction) and then switches to increasing, which marks the onset of dilatancy. The differential stress at which this onset of dilatancy occurs is referred to as C' (Paterson and Wong 2005). We find that (1) the peak stress increases with increasing effective pressure, from ~200 to ~500 MPa as effective pressure is increased from 10 to 50 MPa, (2) the initial nonlinear portion of the stress-strain curves, usually attributed to microcrack closure, is more pronounced at 10 MPa, and (3) the residual differential stress, the frictional sliding stress, increases as a function of effective pressure. The porosity change curves show that porosity first decreases (compaction) during the initial stages of loading, before increasing (dilatancy) as the sample approaches the peak stress. The differential stress values for the onset of inelastic deformation, referred to as C', are 42, 76, and 127 MPa at effective pressures of 10, 30 and 50 MPa, respectively. We measure a large increase in sample porosity following the formation of the macroscopic shear fracture; porosity then increases during sliding on the formed fracture. We note that the decrease in porosity during the initial stages of loading is higher for the sample deformed at 10 MPa, and that the increase in porosity following shear fracture formation decreases as effective pressure increases.

The evolution of permeability as a function of axial strain for the three triaxial experiments shown in Fig. 6 are provided in Fig. 7 (the mechanical data, permeability data and pictures of the deformed samples are available in the Supplementary Information), alongside the stress-strain curves. We first note that the starting permeability (under hydrostatic conditions, before any axial loading is applied, i.e., at a differential stress of 0 MPa) is 1.1×10^{-16}, 1.2×10^{-17}, and 5.3×10^{-18} m^2 at effective pressures of 10, 30, and 50 MPa, respectively. For all three experiments, the permeability decreases as stress is increased up to the peak stress. Following the formation of a macroscopic shear fracture, the permeability increases, before remaining more-or-less constant as the strain is accommodated by sliding on the formed fracture. The permeabilities of the samples at the end of the experiments, following deformation to an axial strain of ~0.1, are 1.4×10^{-17}, 3.3×10^{-18}, and 9.9×10^{-19} m^2 at effective pressures of 10, 30, and 50 MPa, respectively. Therefore, the permeabilities of the samples at the end of the experiments are lower than at the start of the experiments.

4. Discussion

In the following, the evolution of petrophysical properties and microstructure during heating and cooling is first discussed. We then discuss the permeability evolution induced by triaxial compression up to large axial strains in thermally cracked Lanhélin granite and compare these data to the permeability evolution during inelastic deformation of other crystalline and non-crystalline rocks. We relate our results to the evolution of the basement and damage zone adjacent to crustal faults, where past or present activity on the fault promotes stress, displacement and/or strain increases that, in turn, can lead to fracturing. Based on our results, we discuss how the elevated pressure and temperature conditions within these zones might influence permeability. Finally, we use our experimental results to constrain a numerical simulation of fluid flow within a granitic crustal fault system to discuss their potential as geothermal reservoirs.

4.1 The influence of thermal-stressing on the petrophysical properties and microstructure of granite

The in-situ measurements provide additional information to measurements performed periodically on samples during heating and cooling, to help us to better interpret the microstructural and petrophysical changes associated with thermal stressing. For example, the AE and P-wave velocity in-situ measurements performed on Lanhélin granite samples allow us to provide a more precise onset temperature for thermal microcracking and to gain insights into how microcracking progresses throughout heating and cooling. We find that the onset of AE activity, considered a proxy for microcrack growth (Lockner 1993), in Lanhélin granite occurs at ~100 °C and that the number of AE hits continually increases as the granite is heated to 700 °C (Fig. 3). Our data also show that P-wave velocity decreases as temperature increases (P-wave velocity data are only available up to 400 °C due to the maximum working temperature of the P-wave transducers). The onset of AE activity during the heating of granite is observed to be 70−120 °C (Yong and Wang 1980; Hall and Bodnar 1989; Griffiths et al. 2018), in accordance with our onset temperature of ~100 °C for Lanhélin granite. The continuous AE activity as the granite is heated above the onset temperature for thermal microcracking is also in line with previous studies that measured the output of AE during the heating of granite (e.g., Glover et al. 1995; Griffiths et al. 2018). We interpret the AE activity during the heating of Lanhélin granite to be the result of the initiation of growth of thermal microcracks, as observed in our thin section analysis (Fig. 4), and as discussed in the published works mentioned above. Thermal microcracks initiate and grow due to the stresses resulting from the differential thermal expansion of the mineral constituents of the granite (quartz, feldspar, and mica; Figs. 1 and 4, Fredrich and Wong (1986)). This conclusion is corroborated by the measured decrease in P-wave velocity during heating (Fig. 3) and following exposure to high temperature (Fig. 2). Large decreases in the P-wave velocity of granite have been previously observed to result from an increase in thermal microcracking (Reuschlé et al. 2006; Nasseri et al. 2007; Griffiths et al. 2017). The decrease in P-wave velocity as Lanhélin granite is heated to 450 °C, from ~6 to ~3 km.s^{-1}, is similar to the decrease measured in Westerly granite using the same setup and method (Griffiths et al. 2018). Griffiths et al. (2018) found that the P-wave velocity of granite is reduced from ~5 to ~2.5 km.s^{-1} as temperature is increased from room temperature to 450 °C. The noticeable increase in AE activity at ~550–600 °C is considered to be the result of the α/β transition of quartz that occurs at ~573 °C and results in the large volumetric expansion of quartz and therefore an increase in crystal-to-crystal stresses (Glover et al. 1995). Decrepitation of fluid inclusions – cracking at grain-fluid contacts due to thermal stressing – potentially also contributed minorly to the AE activity measured during heating (Hall and Bodnar 1989). For a more systematic investigation of microstructural evolution of granite during thermal stressing, we direct the reader to Meredith et al. (2001).

The cooling of Lanhélin granite is associated with a continuous increase in AE activity and an increase in P-wave velocity (Fig. 3). An increase in P-wave velocity during the cooling of granite was also observed by Griffiths et al. (2018) and was interpreted as the closing of newly formed thermal microcracks that were propped open at high-temperature. However, we also record a continuous increase in AE activity during cooling, as previously observed in experiments performed on granite (Griffiths et al. 2018) and volcanic rocks (Heap et al. 2014; Browning et al. 2016; Daoud et al. 2020; Griffiths et al. 2024). Considering that an increase in thermal microcracking is well-known to reduce the P-wave velocity of granite (Reuschlé et al. 2006; Nasseri et al. 2007; Griffiths et al. 2017), it is very unlikely, based on the P-wave velocity data of Fig. 3, that thermal microcracking is occurring during the cooling of the sample. As discussed in Griffiths et al. (2018), we consider that the majority of the AE hits recorded during the cooling of Lanhélin granite is not associated with newly formed or propagating microcracks, but with the friction on the surfaces of microcracks which partially close up as the rock cools and contracts. We highlight that contemporaneous P-wave velocity measurements are important for the interpretation of AE activity during the heating and cooling of rock samples.

In addition to the observations made using the in-situ measurements, we find that the porosity and permeability of Lanhélin granite increase, whereas P-wave velocity, uniaxial compressive strength, thermal diffusivity, and thermal conductivity decrease as a function of thermal-stressing temperature (Fig. 2). In detail, porosity, strength, thermal diffusivity and conductivity are more-or-less constant below 300°C and then decrease drastically up to 700°C. These changes are interpreted as the consequence of the increase in the number of thermal microcracks as a function of thermal stressing temperature (Fig. 4). Thermal microcracks have previously been observed to decrease the strength and stiffness (Alm et al. 1985; David et al. 2012; Wang et al. 2013; Griffiths et al. 2017; Chen et al. 2017), increase the permeability (Darot et al. 1992; David et al. 1999; Darot and Reuschlé 2000; Chaki et al. 2008), decrease the P-wave velocity (Reuschlé et al. 2006; Nasseri et al. 2007; Chen et al. 2017), and decrease the thermal conductivity (Kant et al. 2007; Zhao et al. 2018) of granite.

4.2 The evolution of permeability during brittle faulting: comparison to other crystalline rocks

We find that the porosity and permeability of thermally-stressed Lanhélin granite decrease as a function of hydrostatic pressure (Fig. 5). These data are in agreement with published data for thermally-stressed granites (Darot et al. 1992; Darot and Reuschlé 2000; Nasseri et al. 2009), and naturally microcracked (Vinciguerra et al. 2005; Fortin et al. 2011) and thermally-stressed basalts (Nara et al. 2011). The reduction in porosity and permeability as a function of effective pressure measured here is interpreted as the result of the progressive closure of thermal microcracks (generated during the thermal treatment to 700 °C; see Fig. 4c).

Under triaxial compression at low confining pressure and room temperature, the permeability of microcracked Lanhélin is found to decrease up to the peak stress and then to increase back to a residual value that remains constant during sliding on the formed shear fracture (Fig. 7). The difference in permeability between intact and faulted samples has been previously measured on low-porosity crystalline rocks in the laboratory. For initially intact La Peyratte granite, Acosta and Violay (2020) reported a decrease in apparent permeability from 6.0×10^{-20} to 1.3×10^{-20} m^2 after hydrostatic loading up to a confining pressure of 25 MPa, and then an increase to 9.0×10^{-20} m^2 following macroscopic brittle failure. Zoback and Byerlee (1975) measured the evolution of the permeability of Westerly granite during triaxial compression (Pc = 25 MPa, Pp = 11 MPa) and showed that the permeability of the deformed sample was twice the permeability of the intact sample. Oda et al. (2002) reported a larger increase in permeability for samples of Inada granite loaded up to brittle failure, where the permeability of the sample post-brittle failure was about two to three orders of magnitude larger than that of the intact granite under the same confining pressure (Pc = 140 MPa).

Critical stress-path dependent permeability variations can also result from microstructural changes that occur in the pre-failure stage of deformation, in particular during the interval between the onset of inelastic deformation C' and macroscopic brittle failure (Faulkner and Armitage 2013). In contrast to our findings on microcracked Lanhélin granite, the permeability of crystalline rocks that initially contain very few microcracks can be significantly higher after failure, by up to several orders of magnitude, compared to the pre-failure state (Oda et al. 2002; Chen et al. 2014; Kluge et al. 2021). In detail, the permeability decreases a little as a result of microcrack closure during the early stages of loading (i.e. at low stress), and then remains almost constant until it starts increasing after the differential stress reaches the critical value required for the onset of inelastic deformation. At stresses higher than the onset of dilatancy, microcracks start forming and propagating and, as they start to coalesce to form a macroscopic shear fracture, large increases in permeability are observed, particularly because permeability is measured in the direction of the crack growth. The permeability of a sample of Odenwald granite deformed at an effective pressure of 20 MPa, for example, was initially equal to 1×10^{-18} m^2, decreased to less than 10^{-18} m^2 as the sample is loaded at low values of stress, before increasing to more than 10^{-17} m^2 when the stress exceeded the critical value for the onset of dilatancy (Kluge et al. 2021). The permeability of the sample of Odenwald granite then increased to more than 10^{-16} m^2 following the stress drops associated with sample failure (Kluge et al. 2021). Similar results were reported by Chen et al. (2014) for Beishan granite samples, whose permeability increased by up to three orders of magnitude during the growth of a cross-cutting shear fracture under triaxial loading at confining pressures of 5, 8, and 10 MPa. In detail, they showed that the relative evolution of permeability during brittle deformation was the same for the different confining pressures but that, at a given differential stress, the higher the confining pressure, the lower the permeability. These results are in agreement with those of Mitchell and Faulkner (2008) for Westerly granite, the permeability of which increased by up to two orders of magnitude as the microfracture density (estimated using image analysis) increased by more than a factor of five during cyclic loading to macroscopic failure.

In comparison, the permeability evolution during triaxial deformation of crystalline rocks initially populated by microcracks is different. For initially microcracked samples, the permeability post-failure is not significantly higher than the pre-failure permeability. In their study, Chen et al. (2017) conducted triaxial deformation tests on Beishan granite samples that were heated to temperatures ranging from 100 to 800 °C prior to deformation. Upon initial loading, the permeability of the samples decreased, and the permeability reduction was more pronounced in samples exposed to higher temperatures (Chen et al. 2017). This may be explained by the fact that the density of thermally induced microcracks increases with the maximum temperature of exposure (Homand-Etienne & Houpert 1989) and, therefore, that the reduction in permeability caused by microcrack closure during the initial loading phase was greater in Beishan granite samples subjected to higher temperatures. As a result of brittle faulting, the permeability of Beishan granite samples thermally-stressed to 100 °C increased by an order of magnitude, whereas the permeability of samples thermally-stressed to 500 °C increased by a factor of two. Inversely, for samples heated to even higher temperatures (600 to 800 °C), the permeability after failure was approximately half of that before failure (Chen et al. 2017). The latter results are similar to those we report here for Lanhélin granite thermally-stressed to 700 °C, which show a permeability decrease following deformation in the brittle regime (Fig. 7). The permeability increase (to a residual value) observed in our samples upon the formation of shear fractures is likely limited by the fact that the fractures formed cut the samples at an angle (30° to the maximum principal stress) and do not connect the top and bottom end of the samples (where the pore fluid flows in and out of the samples). Although the fracture created acts as a preferential conduit for the pore fluid within a limited portion of the overall sample volume, the pore fluid is also required to travel through the remaining undeformed sections of the sample (result of strain localisation, Fig. 6). Consequently, the bulk permeability of the samples, which is governed by the permeability of the different layers within the anisotropic deformed rock (Farquharson and Wadsworth, 2018), did not exhibit a significant increase following the development of the shear fractures.

Our results show the evolution of permeability under compressive loading, including the interval from the onset of dilatancy (when porosity starts to increase, i.e., when the porosity change increases, Figs. 6 and 7) to the peak stress at failure. Typically, this phase is associated with the growth, propagation, and coalescence of microcracks that eventually lead to failure along a cross-cutting shear band (Paterson and Wong 2005). To gain further insight into the dependency of the permeability evolution to the initial microstructural attributes during this interval, we plot the evolution of permeability prior to the formation of a macroscopic shear fracture, termed the "permeability reduction factor" ε (Zhu and Wong 1997; Wong and Zhu 1999), as a function of initial porosity and permeability, where:

$$\varepsilon = \frac{k_{peak}}{k_{C'}} - 1 \qquad (1)$$

k_{peak} and $k_{C'}$ in Equation (1) are the permeabilities of the sample at the peak stress and at the stress for the onset of inelastic deformation C', respectively. Our data for microcracked Lanhélin are plotted alongside compiled data from the literature (for granites, gabbros, sandstones, limestones, and Volvic trachyandesite) in Fig. 8. A value of ε greater than zero indicates that the permeability of the rock increased as it approached macroscopic failure, and a value of ε less than zero indicates that the permeability decreased. Previous studies have defined a porosity threshold of 0.15 for the switch from permeability-increasing to permeability-decreasing behaviour in the brittle regime (Zhu and Wong 1997; Wong and Zhu 1999). Our new data show that a negative permeability reduction factor is possible at a porosity below 0.15 when the porosity consists of a network of microcracks. Fig. 8b shows the permeability reduction factor as a function of the permeability at the onset of inelastic deformation $k_{C'}$. According to this representation, the switch from a permeability-increasing to permeability-decreasing behaviour occurs at a permeability threshold of 10^{-18} m^2. However, more experimental are now required to verify this potential limit and draw firm conclusions on the evolution of permeability during triaxial deformation of initially microcracked rocks. The permeability decreasing behaviour observed for granite samples with initial porosities lower than 0.15 in this study could be explained by (1) the relatively high initial permeability of the microcracked Lanhélin granite compared to other low-porosity crystalline rocks (Fig. 8b) and (2) the fact that the macroscopic fractures formed under triaxial compression developed at an angle and do not connect both ends of the samples (Fig. 7). In comparison to other low-porosity crystalline rocks, the void space of our thermally-stressed granite samples consists of an extensive network of microcracks (Fig. 4) which serves as a relatively efficient pathway for fluid flow despite its relatively small volume. Indeed, our microcracked granite samples exhibit initial permeability values higher than 10^{-18} m^2 – the permeability threshold defined previously – whereas the permeability reported for initially intact low-porosity crystalline rocks such as Inada granite (Oda et al. 2002) or Creighton gabbro (Trimmer et al. 1980) are more than one order of magnitude lower. Despite the thermal microcracks accounting for a small volume within the bulk volume of the sample, their efficiency as fluid pathways results in the sample exhibiting a low porosity but a relatively high permeability. However, the measured increase in permeability due to the development of a macroscopic fracture (Fig. 7) is constrained by the fact that the fracture does not connect the top and bottom of the sample. Therefore, the measured permeability increase does not apparently counterbalance and overcome the decrease in permeability caused by the closure of the pre-existing microcrack network under progressive loading, which is known as one of the most effective processes for permeability reduction (Keaney 1998a).

Overall, our results highlight the importance of initial porosity and permeability and of microcrack density on the evolution of permeability during inelastic deformation prior to failure at low effective pressure (in the brittle regime). During pre-failure inelastic deformation, axial permeability can be significantly reduced in low-porosity crystalline rocks initially populated by thermal microcracks whereas a permeability increase is observed in initially intact low-porosity crystalline rocks.

4.3 Implications for fluid flow and geothermal energy exploitation

In crustal fault systems, micro- and macrocracks that populate the region surrounding the fault core, known as the "damage zone", play a significant role in fluid flow dynamics (Chester and Logan 1986; Wibberley et al. 2008; Faulkner et al. 2010; Mitchell and Faulkner 2012). Our study sheds light on the influence of these micro- and macrocracks on the permeability of granite and therefore serves to study fluid flow in microcracked damage zones typically found around permeable faults and fractures in crustal fault systems.

Fluid flow and convective heat transfer in fault zones are controlled by a combination of geological and physical factors. The permeability ratio between the fault and the surrounding basement is a crucial variable governing the dynamics of convection (López and Smith 1995), which directly affects the intensity, depth, and spatial extent of temperature anomalies (Duwiquet et al. 2019, 2021; Guillou-Frottier et al. 2020). Various processes within fault damage zones enhance permeability compared to the intact basement rock. Tectonic comminution, fluid pressure, and basement alteration are expected to generate fracture networks at different scales, thereby promoting fluid flow (Hagemann et al. 1992; Cassard et al. 1994; Bejan and Lorente 2006; Launay 2019). In our study, the permeability measurements performed after thermal stressing and at different stages of deformation enable us to quantify the potential impact of such processes. To further understand the implications of our findings, we consider a dynamic numerical model with an idealised 3D fault/basement geometry (Fig. 9). The Comsol Multiphysics software was used to model a synthetic vertical fault zone with a thickness of 400 m in a cubic homogeneous basement with 5.5 km-long sides. Thermal insulation was imposed to the vertical faces of the basement and fluid circulation was blocked. A temperature of 20°C and a pressure of 10^5 Pa were imposed to the upper horizontal face. Finally, a heat flux of 100 $\mathrm{mW.m^{-2}}$ (representing the sum of the mantle heat flow and that resulting from the decay of radioactive elements in the underlying crust) was imposed at the base of the model (see Duwiquet et al. 2022 for more details on the simulations). The physical properties measured on the intact, thermally-stressed and deformed Lanhélin granite samples were used to parameterise the simulations (Table 3).

Two simulations were conducted, employing comparable model parameters (Table 3) with the exception of the permeability of the basement surrounding the permeable fault. Fig. 9a illustrates the result obtained when an intact basement surrounding the fault is considered, characterised by a permeability of $kb = 10^{-20}$ m^2 (Table 1). In contrast, Fig. 9b depicts the results for a damaged basement containing both micro- and macrocracks, exhibiting a permeability of $kb = 5 \times 10^{-18}$ m^2 (Table 3). Without any external heat source, the initial temperature distribution used in the simulation follows the average geothermal gradient of the European crust (30 °C/km) (Fink et al. 2022).

The characteristics of the simulated fluid flow within the fault depends on the fault system configuration: a permeable fault surrounded by an intact basement or by a fractured basement. In both cases, where fault permeability is 10^{-14} m^2, the convective motion is observed, with downwelling and upwelling motions contributing to fluid flow. The velocities of the downwelling fluid reach 18×10^{-9} m/s, while at the top of the upwelling motions, the velocities are 4×10^{-9} m/s in the case of a damage zone whereas the velocities reach 19×10^{-9} and 2×10^{-9} m/s, respectively, in the case of an intact basement. Driven by buoyancy forces, these convective flows significantly impact the thermal distribution within the fault. The upwelling motion leads to the rise of the 150 °C isotherm to shallower depths, such as 1.1 km in the middle of the fault in the case of a fractured basement, and 2.2 and 1.1 km on the left and right sides respectively, in the case of an intact basement. Conversely, the downward fluid motion concentrates the 150 °C isotherm at depths of 5.0 km on the left side in the case of a damage zone, and at depths of 3.9 and 4.7 km in the case of an intact basement. In summary, the existence of a fractured basement populated with micro- and macrocracks surrounding the permeable fault enhances convection within the fault system due to its higher permeability, in contrast to a fault system comprised solely of a permeable fault directly surrounded by an intact basement. Since the rocks adjacent to large fault systems are likely cracked on a number of scales, we recommend that future modelling incorporates values for micro- and macrofractured rocks.

These simplified model results show how crustal fault zones with microcracked granitic damage zones around the permeable fault can represent economically viable targets for high-temperature geothermal energy in amagmatic systems. However, it is important to acknowledge that fault zones are subjected to various processes, such as mineralisation, which can reduce permeability and limit fluid flow. Future studies could consider permeability as a dynamic parameter that evolves in time and space, adapted to fractured media, and investigate its variation in relation to triaxial deformation (Fig. 7).

5. Conclusions

In this study, we conducted a comprehensive investigation of the petrophysical and mechanical properties of Lanhélin granite following thermal stressing, and the permeability evolution of thermally microcracked Lanhélin granite during triaxial deformation. Our findings provide insights into the behaviour of granite under various conditions and have implications for understanding fluid flow dynamics in fault zones and the exploitation of geothermal resources.

First, our in-situ measurements during heating and cooling allowed us to observe the onset and progression of thermal microcracking, as indicated by acoustic emission activity and a decrease in P-wave velocity. By observing and analysing their microstructure, we confirmed that thermal microcracks initiate and grow due to the differential thermal expansion of mineral constituents, leading to increases in porosity and permeability and decreases in P-wave velocity, uniaxial compressive strength, thermal diffusivity, and thermal conductivity. Our experiments demonstrated that the porosity and permeability of thermally-stressed granite decrease with increasing hydrostatic pressure, reflecting the closure of thermal microcracks, in agreement with previous studies on microcracked rocks. Second, under triaxial compression at low effective pressure (in the brittle regime), the permeability of microcracked Lanhélin granite decreases following deformation beyond the peak stress. In detail, permeability decreases during loading up to the peak stress and then increases back to a constant residual value upon the development of a shear fracture. Our data revealed that, when the porosity consists of a network of microcracks, a negative permeability reduction factor can be observed at a porosity below 0.15. However, it should be noted that the increase in axial permeability resulting from the growth of shear fractures in our deformed samples was limited by the fact that the shear bands did not extend across the full length of the samples and connect their ends. This limitation, combined with the closure of pre-existing microcracks under progressive loading, led to an overall decrease in permeability. Our results underscore the importance of initial porosity, permeability, and microcrack density in controlling the permeability evolution during inelastic deformation. The behaviour differs for microcracked rocks compared to initially intact low-porosity crystalline rocks, where the latter often exhibit a significant increase in permeability following inelastic deformation and failure in the brittle regime.

Our findings have implications for fluid flow dynamics in crustal fault zones. The presence of micro- and macrocracks in the damage zone can significantly impact permeability, influencing convective heat transfer and temperature anomalies. Our numerical simulations, incorporating the measured petrophysical properties of Lanhélin granite, demonstrated the enhanced convective flow within a fault system when surrounded by a fractured basement compared to an intact basement. Therefore, considering the presence of small deformation features such as microcracks and larger shear fractures surrounding a crustal fault could be crucial for identifying and modelling economically viable targets for geothermal energy in amagmatic systems. Future work should therefore help gathering more experimental data to inform on the evolution of permeability in rocks found in the surrounding of crustal fault zones at high pressure and high temperature.

References

Acosta M, Violay M (2020) Mechanical and hydraulic transport properties of transverse-isotropic Gneiss deformed under deep reservoir stress and pressure conditions. International Journal of Rock Mechanics and Mining Sciences 130:104235. https://doi.org/10.1016/j.ijrmms.2020.104235

Anderson DL (1971) The San Andreas Fault. Sci Am 225:52–71

Baud P, Meredith P, Townend E (2012) Permeability evolution during triaxial compaction of an anisotropic porous sandstone. J Geophys Res Solid Earth 117:5203. https://doi.org/10.1029/2012JB009176

Bauer JF, Krumbholz M, Luijendijk E, Tanner DC (2019) A numerical sensitivity study of how permeability, porosity, geological structure, and hydraulic gradient control the lifetime of a geothermal reservoir. Solid Earth 10:2115–2135. https://doi.org/10.5194/se-10-2115-2019

Bejan A, Lorente S (2006) Constructal theory of generation of configuration in nature and engineering. J Appl Phys 100:. https://doi.org/10.1063/1.2221896/371167

Browning J, Meredith P, Gudmundsson A (2016) Cooling-dominated cracking in thermally stressed volcanic rocks. Geophys Res Lett 43:8417–8425. https://doi.org/10.1002/2016GL070532

Caine JS, Evans JP, Forster CB (1996) Fault zone architecture and permeability structure. Geology 24:1025. https://doi.org/10.1130/0091-7613(1996)024<1025:FZAAPS>2.3.CO;2

Cassard D, Chabod J-C, Marcous E, et al (1994) Mise en place et origine des minéralisations du gisement filonien à Zn, Ge, Ag, (Pb, Cd) de Noailhac - Saint-Salvy (Tarn, France). Chronique de la recherche minière 3–37

Chaki S, Takarli M, Agbodjan WP (2008) Influence of thermal damage on physical properties of a granite rock: Porosity, permeability and ultrasonic wave evolutions. Constr Build Mater 22:1456–1461. https://doi.org/10.1016/j.conbuildmat.2007.04.002

Chandler MR, Meredith PG, Brantut N, Crawford BR (2017) Effect of temperature on the fracture toughness of anisotropic shale and other rocks. Geological Society, London, Special Publications 454:295–303. https://doi.org/10.1144/SP454.6

Chen S, Yang C, Wang G (2017) Evolution of thermal damage and permeability of Beishan granite. Appl Therm Eng 110:1533–1542. https://doi.org/10.1016/j.applthermaleng.2016.09.075

Chen Y, Hu S, Wei K, et al (2014) Experimental characterization and micromechanical modeling of damage-induced permeability variation in Beishan granite. International Journal of Rock Mechanics and Mining Sciences 71:64–76. https://doi.org/10.1016/J.IJRMMS.2014.07.002

Chester FM, Logan JM (1986) Implications for mechanical properties of brittle faults from observations of the Punchbowl fault zone, California. Pure and Applied Geophysics PAGEOPH 124:79–106. https://doi.org/10.1007/BF00875720/METRICS

Cornelio C, Violay M (2020) Parametric analysis of the elastohydrodynamic lubrication efficiency on induced seismicity. Geophys J Int 222:517–525. https://doi.org/10.1093/gji/ggaa180

Daoud A, Browning J, Meredith PG, Mitchell TM (2020) Microstructural Controls on Thermal Crack Damage and the Presence of a Temperature-Memory Effect During Cyclic Thermal Stressing of Rocks. Geophys Res Lett 47:e2020GL088693. https://doi.org/10.1029/2020GL088693

Darot M, Reuschlé T (2000) Acoustic wave velocity and permeability evolution during pressure cycles on a thermally cracked granite. International Journal of Rock Mechanics and Mining Sciences 37:1019–1026. https://doi.org/10.1016/S1365-1609(00)00034-4

David C, Menéndez B, Darot M (1999) Influence of stress-induced and thermal cracking on physical properties and microstructure of La Peyratte granite. International Journal of Rock Mechanics and Mining Sciences 36:433–448. https://doi.org/10.1016/S0148-9062(99)00010-8

David EC, Brantut N, Schubnel A, Zimmerman RW (2012) Sliding crack model for nonlinearity and hysteresis in the uniaxial stress–strain curve of rock. International Journal of Rock Mechanics and Mining Sciences 52:9–17. https://doi.org/10.1016/j.ijrmms.2012.02.001

Duwiquet H, Arbaret L, Guillou-Frottier L, et al (2019) On the geothermal potential of crustal fault zones: a case study from the Pontgibaud area (French Massif Central, France). Geothermal Energy 7:1–29. https://doi.org/10.1186/S40517-019-0150-7/FIGURES/10

Duwiquet H, Guillou-Frottier L, Arbaret L, et al (2021) Crustal Fault Zones (CFZ) as Geothermal Power Systems: A Preliminary 3D THM Model Constrained by a Multidisciplinary Approach. Geofluids 2021:. https://doi.org/10.1155/2021/8855632

Duwiquet H, Magri F, Lopez S, et al (2022) Tectonic Regime as a Control Factor for Crustal Fault Zone (CFZ) Geothermal Reservoir in an Amagmatic System: A 3D Dynamic Numerical Modeling Approach. Natural Resources Research 31:3155–3172. https://doi.org/10.1007/S11053-022-10116-W/FIGURES/7

Farquharson JI, Heap MJ, Lavallée Y, et al (2016) Evidence for the development of permeability anisotropy in lava domes and volcanic conduits. Journal of Volcanology and Geothermal Research 323:163–185. https://doi.org/10.1016/j.jvolgeores.2016.05.007

Faulkner DR, Armitage PJ (2013) The effect of tectonic environment on permeability development around faults and in the brittle crust. Earth Planet Sci Lett 375:71–77. https://doi.org/10.1016/J.EPSL.2013.05.006

Faulkner DR, Jackson CAL, Lunn RJ, et al (2010) A review of recent developments concerning the structure, mechanics and fluid flow properties of fault zones. J Struct Geol 32:1557–1575. https://doi.org/10.1016/j.jsg.2010.06.009

Feng Z jun, Zhao Y sheng, Liu D na (2021) Permeability Evolution of Thermally Cracked Granite with Different Grain Sizes. Rock Mech Rock Eng 54:1953–1967. https://doi.org/10.1007/S00603-020-02361-3/FIGURES/10

Fink J, Heim E, Klitzsch N (2022) Geothermal Potential Across Europe. Springer, Cham, pp 11–27

Fortin J, Stanchits S, Vinciguerra S, Guéguen Y (2011) Influence of thermal and mechanical cracks on permeability and elastic wave velocities in a basalt from Mt. Etna volcano subjected to elevated pressure. Tectonophysics 503:60–74. https://doi.org/10.1016/J.TECTO.2010.09.028

Fredrich JT, Wong T (1986) Micromechanics of thermally induced cracking in three crustal rocks. J Geophys Res Solid Earth 91:12743–12764. https://doi.org/10.1029/JB091IB12P12743

Genter A, Traineau H (1996) Analysis of macroscopic fractures in granite in the HDR geothermal well EPS-1, Soultz-sous-Foreˆts, France. Journal of Volcanology and Geothermal Research 72:121–141. https://doi.org/10.1016/0377-0273(95)00070-4

Glover PWJ, Baud P, Darot M, et al (1995) α/β phase transition in quartz monitored using acoustic emissions. Geophys J Int 120:775–782. https://doi.org/10.1111/J.1365-246X.1995.TB01852.X

Goertz-Allmann BP, Goertz A, Wiemer S (2011) Stress drop variations of induced earthquakes at the Basel geothermal site. Geophys Res Lett 38:2011GL047498. https://doi.org/10.1029/2011GL047498

Griffiths L, Heap MJ, Baud P, Schmittbuhl J (2017) Quantification of microcrack characteristics and implications for stiffness and strength of granite. International Journal of Rock Mechanics and Mining Sciences 100:138–150. https://doi.org/10.1016/j.ijrmms.2017.10.013

Griffiths L, Heap MJ, Lengliné O, et al (2024) Thermal Stressing of Volcanic Rock: Microcracking and Crack Closure Monitored Through Acoustic Emission, Ultrasonic Velocity, and Thermal Expansion. https://doi.org/10.1029/2023JB027766

Griffiths L, Lengliné O, Heap MJ, et al (2018) Thermal Cracking in Westerly Granite Monitored Using Direct Wave Velocity, Coda Wave Interferometry, and Acoustic Emissions. J Geophys Res Solid Earth 123:2246–2261. https://doi.org/10.1002/2017JB015191

Guillou-Frottier L, Carrė C, Bourgine B, et al (2013) Structure of hydrothermal convection in the Upper Rhine Graben as inferred from corrected temperature data and basin-scale numerical models. Journal of Volcanology and Geothermal Research 256:29–49. https://doi.org/10.1016/j.jvolgeores.2013.02.008

Guillou-Frottier L, Duwiquet H, Taillefer A, Roche V (2020) On the morphology and amplitude of 2D and 3D thermal anomalies induced by buoyancy-driven flow within and around fault zones. Solid Earth 11:1571–1595. https://doi.org/10.5194/SE-11-1571-2020

Gustafsson SE (1991) Transient plane source techniques for thermal conductivity and thermal diffusivity measurements of solid materials. Review of Scientific Instruments 62:797–804. https://doi.org/10.1063/1.1142087

Gustavsson M, Karawacki E, Gustafsson SE (1994) Thermal conductivity, thermal diffusivity, and specific heat of thin samples from transient measurements with hot disk sensors. Review of Scientific Instruments 65:3856–3859. https://doi.org/10.1063/1.1145178

Hagemann SG, Groves DI, Ridley JR, Vearncombe JR (1992) The Archean lode gold deposits at Wiluna, Western Australia; high-level brittle-style mineralization in a strike-slip regime. Economic Geology 87:1022–1053. https://doi.org/10.2113/GSECONGEO.87.4.1022

Hall DL, Bodnar RJ (1989) Comparison of fluid inclusion decrepitation and acoustic emission profiles of Westerly granite and Sioux quartzite. Tectonophysics 168:283–296. https://doi.org/10.1016/0040-1951(89)90223-0

Harlé P, Kushnir ARL, Aichholzer C, et al (2019) Heat flow density estimates in the Upper Rhine Graben using laboratory measurements of thermal conductivity on sedimentary rocks. Geothermal Energy 7:38. https://doi.org/10.1186/s40517-019-0154-3

Heap MJ, Jessop DE, Wadsworth FB, et al (2022a) The thermal properties of hydrothermally altered andesites from La Soufrière de Guadeloupe (Eastern Caribbean). Journal of Volcanology and Geothermal Research 421:107444. https://doi.org/10.1016/j.jvolgeores.2021.107444

Heap MJ, Kennedy BM (2016) Exploring the scale-dependent permeability of fractured andesite. Earth Planet Sci Lett 447:139–150. https://doi.org/10.1016/j.epsl.2016.05.004

Heap MJ, Kushnir ARL, Gilg HA, et al (2017) Microstructural and petrophysical properties of the Permo-Triassic sandstones (Buntsandstein) from the Soultz-sous-Forêts geothermal site (France). Geothermal Energy 5:26. https://doi.org/10.1186/s40517-017-0085-9

Heap MJ, Kushnir ARL, Vasseur J, et al (2020) The thermal properties of porous andesite. Journal of Volcanology and Geothermal Research 398:106901. https://doi.org/10.1016/j.jvolgeores.2020.106901

Heap MJ, Lavallée Y, Petrakova L, et al (2014) Microstructural controls on the physical and mechanical properties of edifice-forming andesites at Volcán de Colima, Mexico. J Geophys Res Solid Earth 119:2925–2963. https://doi.org/10.1002/2013JB010521

Heap MJ, Meyer GG, Noël C, et al (2022b) The Permeability of Porous Volcanic Rock Through the Brittle-Ductile Transition. J Geophys Res Solid Earth 127:. https://doi.org/10.1029/2022JB024600

Hicks TW, Pine RJ, Willis-Richards J, et al (1996) A hydro-thermo-mechanical numerical model for HDR geothermal reservoir evaluation. International Journal of Rock Mechanics and Mining Sciences & Geomechanics Abstracts 33:499–511. https://doi.org/10.1016/0148-9062(96)00002-2

Homand-Etienne F, Houpert R (1989) Thermally induced microcracking in granites: characterization and analysis. International Journal of Rock Mechanics and Mining Sciences & Geomechanics Abstracts 26:125–134. https://doi.org/10.1016/0148-9062(89)90001-6

Huenges E, Ledru P (2011) Geothermal energy systems: exploration, development, and utilization. John Wiley & Sons

Jónsson S, Segall P, Pedersen R, Björnsson G (2003) Post-earthquake ground movements correlated to pore-pressure transients. Nature 424:179–183. https://doi.org/10.1038/nature01776

Kant MA, Ammann J, Rossi E, et al (2017) Thermal properties of Central Aare granite for temperatures up to 500°C: Irreversible changes due to thermal crack formation. Geophys Res Lett 44:771–776. https://doi.org/10.1002/2016GL070990

Keaney GMJ (1998) Experimental Study of the Evolution of Permeability in Rocks Under Simulated Crustal Stress Conditions. UCL

Keaney GMJ, Meredith PG, Murrell SAF (1998) Laboratory Study of Permeability Evolution in a Tight' Sandstone under Non-Hydrostatic Stress Conditions. In: All Days. SPE

Kluge C, Blöcher G, Barnhoorn A, et al (2021) Permeability Evolution During Shear Zone Initiation in Low-Porosity Rocks. Rock Mech Rock Eng 54:5221–5244. https://doi.org/10.1007/S00603-020-02356-0/FIGURES/15

Kranz RL (1983) Microcracks in rocks: A review. Tectonophysics 100:449–480. https://doi.org/10.1016/0040-1951(83)90198-1

Launay G (2019) Hydrodynamique des systèmes minéralisés péri-granitiques : étude du gisement à W-Sn-(Cu) de Panasqueira (Portugal). Thèse, Université d'Orléans

Li Z, Wong LNY, Teh CI (2020) Influence of Thermal and Mechanical Loading on Development of Microcracks in Granite. Rock Mech Rock Eng 53:2035–2051. https://doi.org/10.1007/S00603-019-02030-0/FIGURES/14

Lockner D (1993) The role of acoustic emission in the study of rock fracture. International Journal of Rock Mechanics and Mining Sciences & Geomechanics Abstracts 30:883–899. https://doi.org/10.1016/0148-9062(93)90041-B

López DL, Smith L (1995) Fluid Flow in Fault Zones: Analysis of the Interplay of Convective Circulation and Topographically Driven Groundwater Flow. Water Resour Res 31:1489–1503. https://doi.org/10.1029/95WR00422

Meng F, Baud P, Ge H, Wong T fong (2019) The Effect of Stress on Limestone Permeability and Effective Stress Behavior of Damaged Samples. J Geophys Res Solid Earth 124:376–399. https://doi.org/10.1029/2018JB016526

Meredith PG, Knight KS, Boon SA, Wood IG (2001) The microscopic origin of thermal cracking in rocks: An investigation by simultaneous time-of-flight neutron diffraction and acoustic emission monitoring. Geophys Res Lett 28:2105–2108. https://doi.org/10.1029/2000GL012470

Mitchell TM, Faulkner DR (2008) Experimental measurements of permeability evolution during triaxial compression of initially intact crystalline rocks and implications for fluid flow in fault zones. J Geophys Res 113:B11412. https://doi.org/10.1029/2008JB005588

Mitchell TM, Faulkner DR (2012) Towards quantifying the matrix permeability of fault damage zones in low porosity rocks. Earth Planet Sci Lett 339–340:24–31. https://doi.org/10.1016/j.epsl.2012.05.014

Nara Y, Kato M, Niri R, et al (2018) Permeability of Granite Including Macro-Fracture Naturally Filled with Fine-Grained Minerals. Pure Appl Geophys 175:917–927. https://doi.org/10.1007/s00024-017-1704-x

Nasseri MHB, Schubnel A, Young RP (2007) Coupled evolutions of fracture toughness and elastic wave velocities at high crack density in thermally treated Westerly granite. International Journal of Rock Mechanics and Mining Sciences 44:601–616. https://doi.org/10.1016/j.ijrmms.2006.09.008

Noël C, Passelègue FX, Violay M (2021) Brittle Faulting of Ductile Rock Induced by Pore Fluid Pressure Build-Up. J Geophys Res Solid Earth 126:. https://doi.org/10.1029/2020JB021331

Oda M, Takemura T, Aoki T (2002) Damage growth and permeability change in triaxial compression tests of Inada granite. Mechanics of Materials 34:313–331. https://doi.org/10.1016/S0167-6636(02)00115-1

Paterson MS, Wong T (2005) Experimental Rock Deformation: The Brittle Field, 2nd Edition. Springer Verlag

Pimienta L, Orellana LF, Violay M (2019) Variations in Elastic and Electrical Properties of Crustal Rocks With Varying Degree of Microfracturation. J Geophys Res Solid Earth 124:6376–6396. https://doi.org/10.1029/2019JB017339

Rawling GC, Goodwin LB, Wilson JL (2001) Internal architecture, permeability structure, and hydrologic significance of contrasting fault-zone types. Geology 29:43. https://doi.org/10.1130/0091-7613(2001)029<0043:IAPSAH>2.0.CO;2

Reuschlé T, Gbaguidi Haore S, Darot M (2006) The effect of heating on the microstructural evolution of La Peyratte granite deduced from acoustic velocity measurements. Earth Planet Sci Lett 243:692–700. https://doi.org/10.1016/j.epsl.2006.01.038

Sibson RH (1996) Structural permeability of fluid-driven fault-fracture meshes. J Struct Geol 18:1031–1042. https://doi.org/10.1016/0191-8141(96)00032-6

Siratovich PA, Villeneuve MC, Cole JW, et al (2015) Saturated heating and quenching of three crustal rocks and implications for thermal stimulation of permeability in geothermal reservoirs. International Journal of Rock Mechanics and Mining Sciences 80:265–280. https://doi.org/10.1016/j.ijrmms.2015.09.023

Terakawa T, Miller SA, Deichmann N (2012) High fluid pressure and triggered earthquakes in the enhanced geothermal system in Basel, Switzerland. J Geophys Res Solid Earth 117:n/a-n/a. https://doi.org/10.1029/2011JB008980

Trimmer D, Bonner B, Heard HC, Duba A (1980) Effect of pressure and stress on water transport in intact and fractured gabbro and granite. J Geophys Res Solid Earth 85:7059–7071. https://doi.org/10.1029/JB085IB12P07059

Vallier B, Magnenet V, Schmittbuhl J, Fond C (2019) Large scale hydro-thermal circulation in the deep geothermal reservoir of Soultz-sous-Forêts (France). Geothermics 78:154–169. https://doi.org/10.1016/j.geothermics.2018.12.002

Villeneuve MC, Heap MJ, Kushnir ARL, et al (2018) Estimating in situ rock mass strength and elastic modulus of granite from the Soultz-sous-Forêts geothermal reservoir (France). Geothermal Energy 6:11. https://doi.org/10.1186/s40517-018-0096-1

Vinciguerra S, Trovato C, Meredith PG, Benson PM (2005) Relating seismic velocities, thermal cracking and permeability in Mt. Etna and Iceland basalts. International Journal of Rock Mechanics and Mining Sciences 42:900–910. https://doi.org/10.1016/J.IJRMMS.2005.05.022

Wadsworth FB, Heap MJ, Damby DE, et al (2017) Local geology controlled the feasibility of vitrifying Iron Age buildings. Sci Rep 7:40028. https://doi.org/10.1038/srep40028

Wang C-Y, Manga M (2021) Earthquakes Influenced by Water. pp 61–82

Wang Y, Cao M, Zhao Y, et al (2013) Experimental Investigations on Microcracks in Vibrational and Conventional Drilling of Cortical Bone. J Nanomater 2013:1–5. https://doi.org/10.1155/2013/845205

Wibberley CAJ, Yielding G, Di Toro G (2008) Recent advances in the understanding of fault zone internal structure: A review. Geol Soc Spec Publ 299:5–33. https://doi.org/10.1144/SP299.2/ASSET/672AFC80-80DF-4C9E-87B2-46A48D196891/ASSETS/IMAGES/LARGE/1374CH02F09.JPG

Wong T, Zhu W (1999) Brittle faulting and permeability evolution: Hydromechanical measurement, microstructural observation, and network modeling. GMS 113:83–99. https://doi.org/10.1029/GM113P0083

Xu JJ, Zhang YH, Rutqvist J, et al (2023) Thermally Induced Microcracks in Granite and Their Effect on the Macroscale Mechanical Behavior. J Geophys Res Solid Earth 128:e2022JB024920. https://doi.org/10.1029/2022JB024920

Yin J, Yu D, Yin Z, et al (2015) Modelling the anthropogenic impacts on fluvial flood risks in a coastal mega-city: A scenario-based case study in Shanghai, China. Landsc Urban Plan 136:144–155. https://doi.org/10.1016/j.landurbplan.2014.12.009

Yong C, Wang C -y (1980) Thermally induced acoustic emission in westerly granite. Geophys Res Lett 7:1089–1092. https://doi.org/10.1029/GL007I012P01089

Yu X, Xu T, Heap MJ, et al (2021) Time-dependent deformation and failure of granite based on the virtual crack incorporated numerical manifold method. Comput Geotech 133:104070. https://doi.org/10.1016/j.compgeo.2021.104070

Zhao XG, Zhao Z, Guo Z, et al (2018) Influence of Thermal Treatment on the Thermal Conductivity of Beishan Granite. Rock Mech Rock Eng 51:2055–2074. https://doi.org/10.1007/s00603-018-1479-0

Zhu W, Wong T (1997) The transition from brittle faulting to cataclastic flow: Permeability evolution. J Geophys Res Solid Earth 102:3027–3041. https://doi.org/10.1029/96JB03282

Zoback MD, Byerlee JD (1975) The effect of microcrack dilatancy on the permeability of westerly granite. J Geophys Res 80:752–755. https://doi.org/10.1029/JB080I005P00752

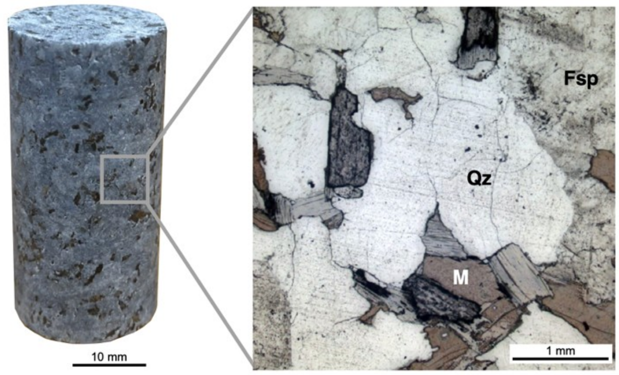

Fig. 1 Photograph of a cylindrical (20 mm in diameter) Lanhélin granite sample and optical microscope image (taken in reflected light) of the intact microstructure, where quartz (Qz), feldspar (Fsp), and mica (M) crystals can be observed.

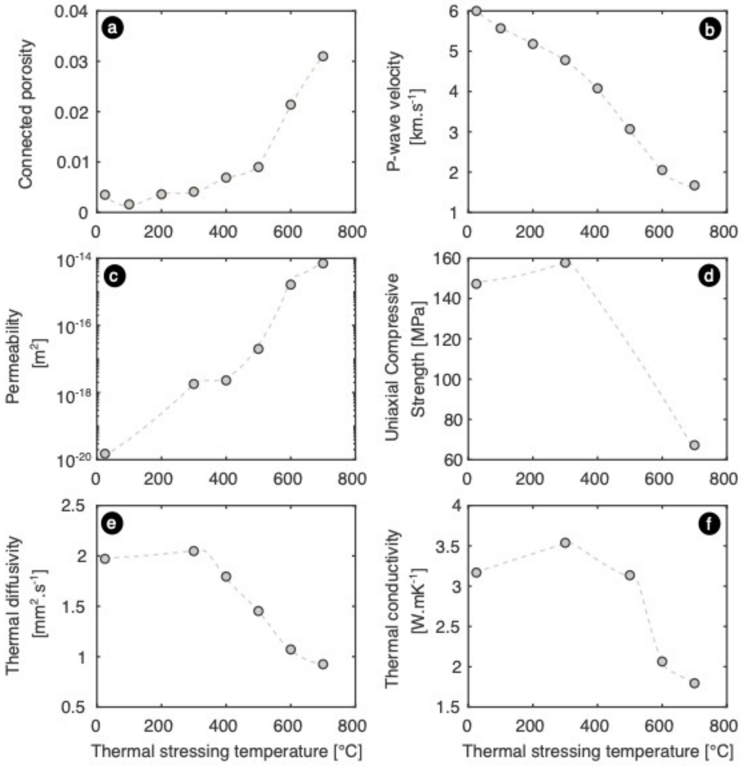

Fig. 2 Evolution of petrophysical properties following the thermal stressing of Lanhélin granite to 700 °C (measurements made at room temperature). (a) Connected porosity, (b) P-wave velocity, (c) permeability, (d) uniaxial compressive strength, (e) thermal diffusivity, and (f) thermal conductivity are given as a function of thermal-stressing temperature. Little variations are attributed to natural variability between the different granite samples used for the measurements at each temperature. Data are given in Table 1.

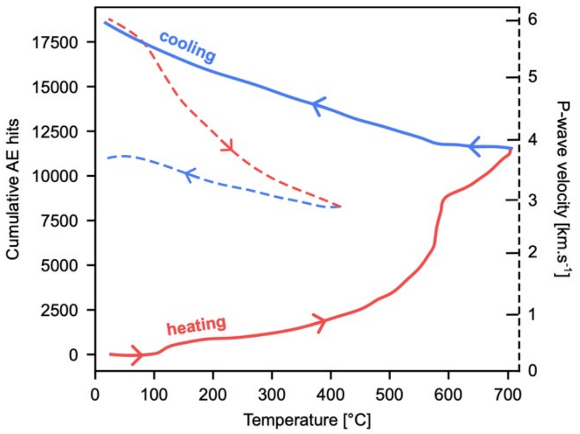

Fig. 3 Acoustic emissions (AE) (solid lines) during a heating-cooling cycle from 20 to 700 °C and in-situ P-wave velocity (dashed lines) during a heating-cooling cycle from 20 to 450 °C for Lanhélin granite. Heating and cooling curves are shown in red and blue, respectively. AEs were recorded continuously using a 40 dB detection threshold. P-wave velocities were measured every 10 seconds during the heating-cooling cycle. While AE could be measured using sensors outside the furnace, the transducers for velocity measurements were placed inside the furnace, which ensured good quality in the data but limited the maximum temperature that could be used.

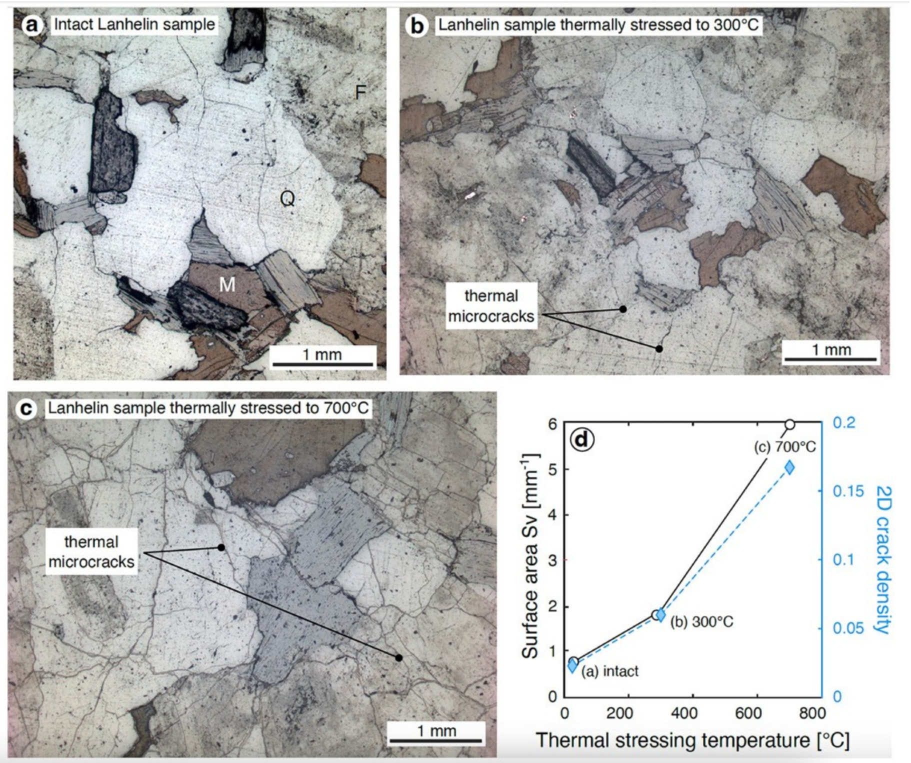

Fig. 4 Microstructural evolution of Lanhélin granite following thermal stressing to 700 °C. An optical microscope image (taken in reflected light) of (a) the intact microstructure, (b) the microstructure following exposure to 300 °C, and (c) the microstructure following exposure to 700 °C. These images were analysed using the crack-counting method presented in Griffiths et al. (2017) to determine (d) the evolution of surface area per unit volume (open circles) and 2D crack density (blue diamonds) as a function of thermal-stressing temperature.

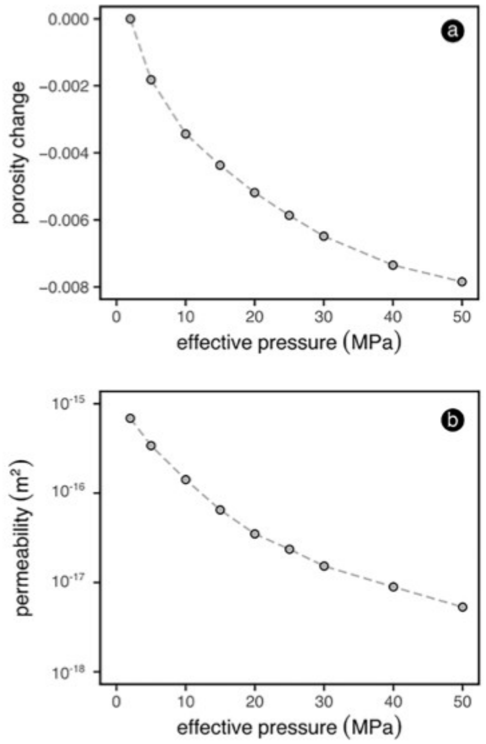

Fig. 5 Porosity change (a) and permeability (b) as a function of effective pressure during the hydrostatic pressurisation of thermally-stressed (to 700 °C) Lanhélin granite. Data are given in Table 2.

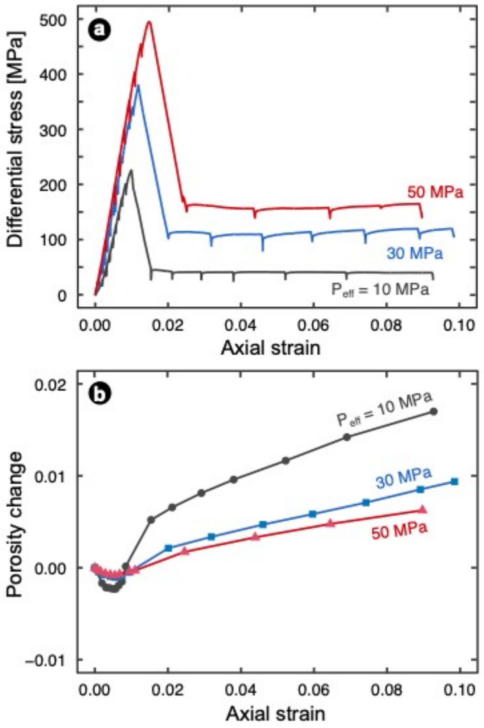

Fig. 6 Mechanical data for the triaxial compression of thermally-stressed (to 700 °C) Lanhélin granite in the brittle regime. (a) Differential stress and (b) porosity change are presented as a function of axial strain for tests performed at effective pressures of 10 MPa (black lines), 30 MPa (blue lines), and 50 MPa (red lines). Several stages can be observed on the stress-strain curves. First, the elastic deformation of the sample. Then, the inelastic deformation: dilatancy takes place by opening and propagation of microcracks and ultimately, as the microcracks coalesce into a macroscopic fracture, brittle failure occurs as stress reaches its peak value. Lastly, mechanical data show a stage

during which stress remains more-or-less constant as deformation is accommodated by sliding on the formed fracture. An Excel file containing all the mechanical data is provided in the Supplementary Information.

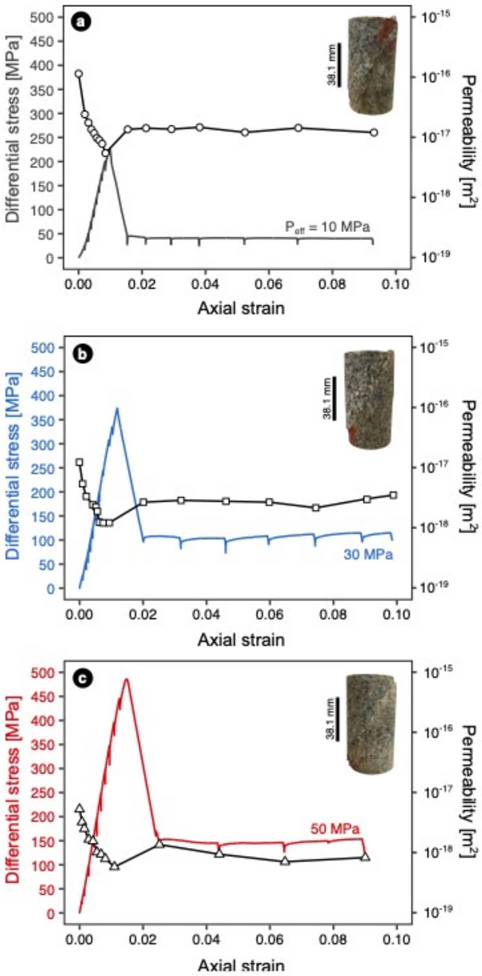

Fig. 7 Evolution of the permeability of thermally-stressed (to 700 °C) Lanhélin granite during deformation in the brittle regime. Mechanical data (solid lines) and permeability (dashed lines) are presented as a function of axial strain for triaxial experiments performed at effective pressures of (a) 10 MPa, (b) 30 MPa, and (c) 50 MPa. Photographs of the post-deformation samples are included in the top right corner of each panel. Larger version of these photographs and an Excel file containing all the mechanical data and permeability data are provided in the Supplementary Information.

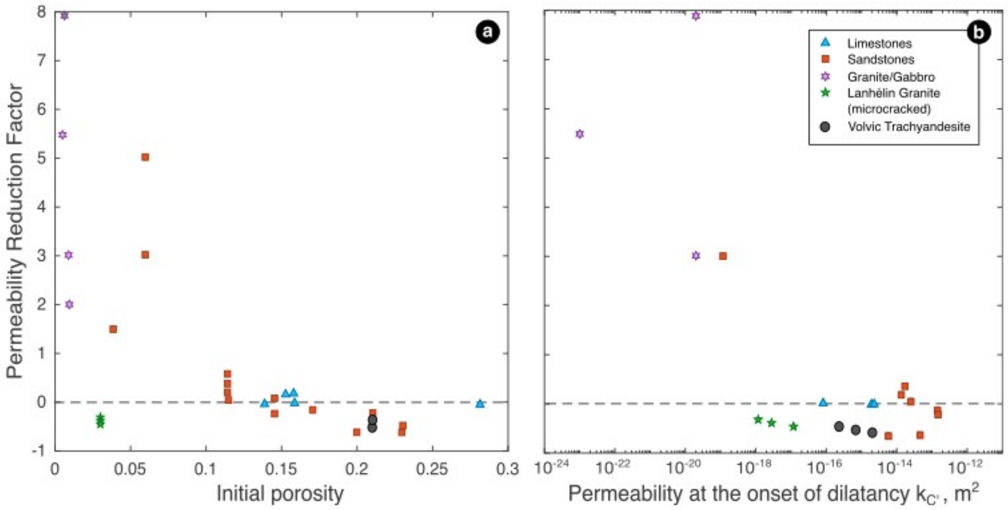

Fig. 8 Permeability reduction factor (see Equation 1) as a function of (a) initial porosity and (b) permeability at the onset of inelastic deformation for microcracked Lanhélin granite (green stars) and compiled data for limestones (blue triangles; data from Meng et al. 2019), sandstones (red squares; data from (Zhu and Wong 1997; Keaney et al. 1998; Wong and Zhu 1999; Baud et al. 2012), granites and gabbros (purple stars; data from (Zoback and Byerlee 1975; Trimmer et al. 1980), and trachyandesite (black circles; data from Heap et al. (2022).

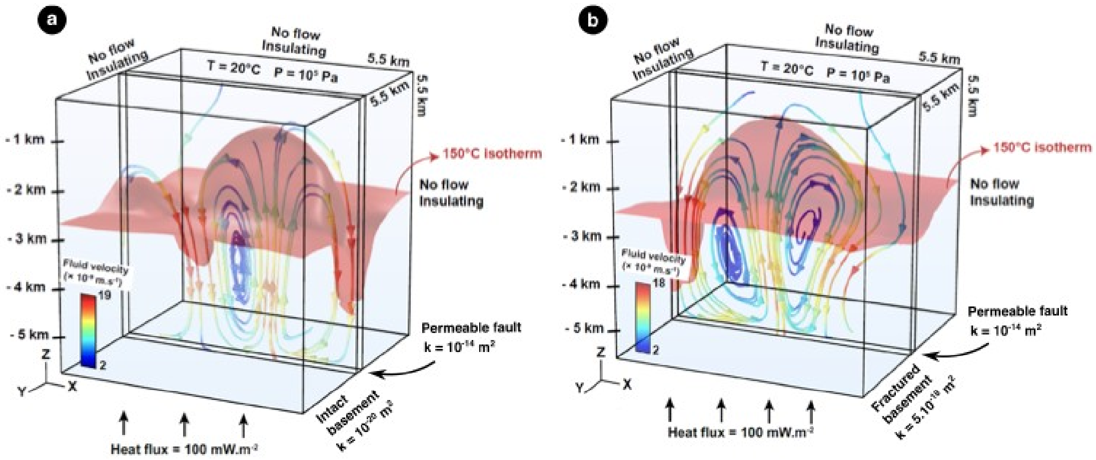

Fig. 9 Simulated fluid flow within a crustal fault zone system consisting of (a) a permeable fault surrounded by intact basement rock and (b) a permeable fault surrounded by a fractured basement, populated with micro- and macrocracks. The numerical simulation results represent the steady state condition, after 10 000 years. The 150 °C isotherm is highlighted by the pink surface. Fluid flow is marked by streamlines, where the red colour corresponds to the highest velocity and the blue colour to the lowest. A detailed description of the method used for the numerical simulations is given in Duwiquet et al. (2022).

Sample	Thermal stressing temperature (°C)	Connected porosity	P-wave velocity (km.s^{-1})	Permeability (m^2)	UCS (MPa)	Thermal diffusivity (mm^2.s^{-1})	Thermal conductivity (W.mK^{-1})
LG1	RT	0.0035	6.00	1.50×10^{-20}	147	1.97	3.17
LG2	100	0.0016	5.57	-	-	-	-
LG3	200	0.0036	5.18	-	-	-	-
LG4	300	0.0041	4.78	1.80×10^{-18}	158	2.05	3.54
LG5	400	0.0069	4.08	2.30×10^{-18}	-	1.80	2.52
LG6	500	0.0090	3.07	1.99×10^{-17}	-	1.45	3.14
LG7	600	0.0214	2.05	1.64×10^{-15}	-	1.07	2.06
LG8	700	0.0310	1.67	7.05×10^{-15}	67	0.92	1.79

Table 1 Connected porosity, P-wave velocity, permeability, uniaxial compressive strength (UCS), thermal diffusivity, and thermal conductivity data for Lanhélin granite as a function of thermal-stressing temperature. Permeability, UCS and thermal properties were voluntarily measured only for selected thermal stressing temperatures. RT - room temperature. Mechanical data for the UCS tests are included in Supplementary Information.

Effective pressure (MPa)	Porosity change	Permeability (m^2)
2	0	6.9×10^{-16}
5	−0.00182	3.4×10^{-16}
10	−0.00344	1.4×10^{-16}
15	−0.00437	6.5×10^{-17}
20	−0.00518	3.5×10^{-17}
25	−0.00587	2.4×10^{-17}
30	−0.00649	1.5×10^{-17}
40	−0.00735	8.9×10^{-18}
50	−0.00785	5.3×10^{-18}

Table 2 Porosity change and permeability data as a function of effective pressure during the hydrostatic pressurisation of thermally-stressed (to 700 °C) Lanhélin granite. The pore pressure used in the experiment was 10 MPa.

Parameters	**Symbols**	**Values**	**Units**
Density	ρs	2700	kg/m^3
Fault porosity	φf	0.10	-
Basement porosity	φb	0.05	-
Fault permeability	kf	10^{-14}	m^2
Intact basement permeability	kb	10^{-20}	m^2
Fractured basement permeability	kd	5×10^{-18}	m^2
Thermal conductivity	λs	3.54	W/(m.K)
Thermal capacity	Cpa	1000	K/(kg.K)
Thermal expansion coefficient	β	7×10^{-6}	1 /K
Fluid variables and parameters			
Fluid density	ρf	1036.5 – 0.14167 × (T-273.15) – 0.0022381 × (T – 273.15) × (T – 273.15)	kg/m^3
Thermal conductivity	λf	0.60	W/(m.K)
Thermal capacity	Cpf	4100	J/(kg.K)
Thermal expansion coefficient	α	10^{-4}	1/K
Fluid dynamic viscosity	μ	2.414×10^{-5} exp(570/((T-273.15)+133))	Pa.s

Table 3 Rock and fluid parameters used in the numerical simulations, derived from measurements made on intact, thermally-stressed, and deformed Lanhélin granite in this study.